Long-ranged formation of the Bicoid gradient requires multiple dynamic modes that spatially vary across the embryo

Thamarailingam Athilingam[1], Ashwin V.S. Nelanuthala[2], Catriona Breen[3,+], Thorsten Wohland[2,4,*], and Timothy E. Saunders[1,2,5,*,#]

[1] Mechanobiology Institute, National University of Singapore, Singapore 117411
[2] Department of Biological Sciences and Centre for Bioimaging Sciences, National University of Singapore, Singapore 117558
[3] Cornell University, Ithaca, NY, USA 14850
[4] Department of Chemistry, National University of Singapore, Singapore 117558
[5] Warwick Medical School, University of Warwick, Coventry, CV4 7AL, United Kingdom
* For correspondence: twohland@nus.edu.sg , timothy.saunders@warwick.ac.uk
[#] Lead contact
[+] Present address: Department of Organismic and Evolutionary Biology, Museum of Comparative Zoology, Harvard University, Cambridge, MA, USA 02138

Abstract

Morphogen gradients provide essential positional information to downstream gene networks through their spatially heterogeneous distribution. Yet, how morphogen gradients form is still hotly contested, with multiple models proposed for different systems. Here, we focus on the transcription factor Bicoid (Bcd), a morphogen that forms an exponential gradient across the anterior-posterior (AP) axis of the early *Drosophila* embryo. We utilise fluorescence correlation spectroscopy (FCS) and perturbations to Bcd, to dissect Bcd dynamics at multiple spatial and temporal locations across the embryo. In both the cytoplasm and nucleus, we find two dynamic modes for Bicoid diffusion dynamics, consisting of fast and slow populations of Bcd. Surprisingly, there are spatial differences in Bcd diffusivity along the AP-axis, with Bcd diffusing more rapidly in the posterior. In the nucleus, we demonstrate that the slower mode of Bcd transport is due to Bcd DNA binding. Addition of the Bcd homeodomain to eGFP::NLS can qualitatively replicate the observed Bcd concentration profile, suggesting this domain is the primary region regulating Bcd dynamics. This study provides a detailed analysis of morphogen dynamics at different spatial and temporal locations, revealing multiple modes of transport. These results explain how a long-ranged gradient can form while retaining a steep profile through much of its range.

Keywords: Fluorescence correlation spectroscopy, Bicoid, *Drosophila* embryo, morphogens, diffusion

Introduction

Morphogens are signalling molecules that provide crucial spatial and temporal information to cells during development.[1,2] Knowing how morphogen gradients form and on what time scales

is essential for understanding how information can be precisely decoded.[3-5] Despite intensive study, the underlying dynamics of morphogen gradient formation remain controversial.[6-9] A longstanding model is that morphogen gradients are formed by localised synthesis and diffusive processes combined with protein degradation or trapping (the SDD model).[4,5,10,11] Alternative hypotheses for generating a long-ranged gradient include distributed sources of morphogen[12,13] and long-ranged transport via cytonemes.[14,15] The shape of the morphogen profile can be adjusted by the mode of degradation,[5,16,17] which may make the gradient more robust to variation in morphogen protein levels.[16,18,19] The morphogen profile can also be modulated through receptor binding.[8,20]

A range of quantitative techniques have been used to measure morphogen dynamics *in vivo.* These include fluorescence correlation spectroscopy (FCS),[5,21-23] fluorescence recovery after photobleaching (FRAP),[4] single molecule tracking,[24,25] and protein lifetime measurements.[26-28] FRAP and protein lifetime measurements provide insight into the longer time dynamics of the system. Essentially, they average out sub-second processes, giving a measure of the effective dynamic parameters across the system. FCS and single molecule imaging have the advantage of measuring the local fast dynamics, but often do not provide information about longer time and spatial processes. See Refs 9 and 17 for an extended discussion on these points. These differences have led to conflict in the measured dynamic parameters for morphogens. For example, the reported diffusion constant for eGFP::Bcd can vary from 0.4 $\mu m^2/s$ (FRAP)[4] to 7 $\mu m^2/s$ (FCS).[29] While theoretical work has looked to integrate these measurements, taking account of the different time scales measured,[30] there remains significant contention over the Bcd dynamics. Similar issues are pertinent in other morphogen systems, such as Nodal[22,31,32] and Wingless.[8,33] Finally, analysis of morphogen dynamics has typically focused on a fluorescently-tagged version of the wildtype morphogen protein. There is a lack of quantitative data on how morphogen dynamics are altered when protein domains – *e.g.*, DNA or receptor binding motifs - are perturbed. Despite intense study over the past twenty years, it remains a major challenge to dissect the multiple time and spatial scales that underlie morphogen dynamics and the mechanisms that shape the gradient; such knowledge is essential for understanding of how morphogens gradients form *in vivo.*[8]

Here, we take advantage of FCS combined with new reagents for live imaging to dissect the dynamics of Bcd with unprecedented precision. Using this, we reveal, with high accuracy, the dynamic modes that generate the Bcd gradient. We measure the Bcd dynamics at multiple locations along the embryo AP-axis and through nuclear cycles (n.c.) 12-14. We demonstrate that Bcd dynamics do not substantially change over n.c. 12-14, contrary to previous claims.[34] A two-component fit to the FCS curves is substantially better than a one-component fit in both the cytoplasm and nucleus; this implies two ("slow" and "fast") dynamic modes in each region. The dynamics of the slower mode correspond closely to measured Bcd dynamics from FRAP. We show that the effective diffusion coefficient varies across the embryo, with the effective diffusion coefficient increasing towards the posterior. We explored eGFP::Bcd dynamics in a mutant with disrupted DNA binding. Loss of DNA binding increases the fraction of eGFP::Bcd in the fast dynamic mode within the nucleus. In the cytoplasm, we demonstrate that the Bcd

homeodomain plays a role in regulating Bcd diffusivity. Combining the Bcd homeodomain with an eGFP::NLS can reproduce the dynamics and gradient shape of the eGFP::Bcd gradient. These results reveal that Bcd gradient formation is substantially more complicated than previously considered and provide a potential explanation – via the presence of multiple dynamic modes - for how long-ranged gradients can form across large distances in relative short periods of time.

Results

Bicoid dynamics do not vary from n.c. 12 to early n.c. 14 and are described by two dynamic modes in both the nuclei and cytoplasm

Previously, confocal FCS was used to measure the diffusion coefficients of eGFP::Bcd in the anterior cytoplasm[29] and in anterior nuclei.[35] These measurements were limited in their position and timing within the embryo. We revisited these results, expanding the FCS measurements to both the anterior and posterior regions of the embryo during the interphases of n.c. 12, 13 and 14 (Figure 1A-B, Figure S1A-B). Our FCS autocorrelation curves were highly reproducible between embryos (Figure S1C). We also co-imaged our eGFP::Bcd with H2A::mCherry to ensure that we precisely determined n.c. and the cytoplasmic and nuclear regions.

Comparing the normalised FCS autocorrelation curves of cytoplasm and nuclei in n.c. 12-14 (Figure 1B, Figure S1C), we saw no clear differences in the curves within or between cycles during interphase. These results reveal that the dynamics of eGFP::Bcd is relatively stable through n.c. 12-14 both at the anterior and posterior locations of the embryo. This contrasts with previous claims based on imaging the Bcd profile within nuclei, which predicted very small Bcd diffusion, D<1μm^2/s.[34] We did not explore the dynamics during mitosis with point FCS as the nuclei (chromatin) move rapidly during this phase.

We next fitted dynamic models to the averaged autocorrelation curves (Figure 1C-D). We found that a one-component model of diffusion is insufficient (Figure S1D-E), but a two-component diffusive model (with a fast and slow diffusing population) fits the data well in all cases (Figure 1C-D). We define the effective diffusion coefficient as $D_{eff} = f_{fast}D_{fast} + f_{slow}D_{slow}$, where D_{fast} and f_{fast} represent the diffusion coefficient and fraction for the fast dynamic mode (and similarly for the slow dynamic mode), with $f_{fast} + f_{slow} = 1$. We found the effective diffusion coefficients of eGFP::Bcd in the anterior cytoplasm and nuclei were 7-9 μm^2/s and 4-6 μm^2/s respectively (Figure 1E), consistent with previous observations.[29,35] Further, from FCS we can estimate the local eGFP::Bcd concentration (Figure 1F, Methods) and these measures map onto previous results.[4,29] Therefore, we are confident our results are reproducible and reflect accurate measurements of the eGFP::Bcd interphase dynamics.

Bicoid dynamics spatially vary along the embryo anterior-posterior axis

We analysed the effective diffusion coefficient in different regions of the embryo. Strikingly, for both nuclear and cytoplasmic eGFP::Bcd, the effective diffusivity was larger in the posterior of the embryo compared with the anterior (Figure 1E). In the posterior, the effective eGFP::Bcd diffusion coefficient in the cytoplasm and nuclei ranged from 12-15 $\mu m^2/s$ and 7-10 $\mu m^2/s$ respectively (Table S1 and S2), a ~1.7 fold increase in the posterior (Figure S1F). We confirmed that this result was valid even if each n.c. was analysed separately (Figure S1G). This effective diffusion was inversely correlated with eGFP::Bcd concentration (Figure 1E and F).

Exploring the different dynamic modes for eGFP::Bcd (Figure 1G-G'), we see that in the cytoplasm, the slow dynamic mode is similar across the embryo, $\sim 1\ \mu m^2/s$ (Figure 1G'). The fast mode shows an increased diffusivity from $D_{fast}\ (anterior) = 13.0 \pm 2.6\ \mu m^2/s$ to $D_{fast}\ (posterior) = 18.8 \pm 2.5\ \mu m^2 s$ (Figure 1G, Table S1). In the nuclei, eGFP::Bcd shows a significant, though small, increase in diffusivity in the fast dynamic mode from anterior to posterior regions (9 to 12 $\mu m^2/s$ respectively), with the slow component remaining unchanged (Figure 1G, Table S2).

We next asked whether the relative fractions of slow and fast components change along the embryo AP-axis. In the anterior cytoplasm, the faster diffusing species comprised $f_{fast} = 65 \pm 8$ %, whereas in the posterior this is increased to $f_{fast} = 78 \pm 6$ % (Figure 1H, Table S1). Although the slow cytoplasmic dynamic mode is similar in both anterior and posterior of the embryo, the effective diffusion increased towards the posterior because (i) the fast dynamic mode is quicker and (ii) the fraction of the eGFP::Bcd in the fast mode is larger. Likewise, in the nucleus the fraction of eGFP::Bcd in the faster dynamic mode increases towards the posterior, thereby increasing the effective diffusion coefficient (Figure 1H).

We performed a similar analysis for eGFP::NLS, driven off the Bcd promoter region. We again fitted with a two-component diffusive model. The majority of the cytoplasmic eGFP::NLS is in the faster diffusive mode (Figure S2). There is a small difference in the eGFP::NLS dynamics in the nuclei between anterior and posterior ends, possibly due to crowding/non-specific interaction effects in the anterior where protein number is higher (Figure S2F-H'). Supporting this, we see in the anterior nuclei a small but significant fraction (~20%) of eGFP::NLS in a slower mode (Figure S2I, Table S2). Overall, we see that eGFP::NLS diffusion is more rapid, with 80-95% existing in the faster diffusive mode. This is consistent with eGFP::NLS only weakly interacting with other components (*e.g.* itself or DNA binding and cytoplasmic elements).

In summary, the dynamics of eGFP::Bcd varies across the embryo, both in terms of the magnitude of the diffusivity and the fraction of slow and fast diffusing eGFP::Bcd. This means that the classic SDD model needs to be revisited as the dynamics are dependent on the spatial location and/or the local morphogen concentration within the embryo.

Bicoid DNA binding determines the slow transport mode within the nucleus

Given our above observations, we investigated the possible mechanisms regulating Bcd diffusivity. First, we focused on Bcd dynamics within the nucleus. Bcd is a transcription factor[36] and known to cooperatively bind to DNA.[37,38] Therefore, we hypothesised that direct DNA binding determines the slow Bcd transport mode in the nucleus.

The Bcd homeodomain mutation *bcd*^{N51A} leads to loss of downstream target expression (*e.g. hunchback*) posited due to a disruption of Bcd DNA binding efficacy.[39] It also has a reported role in *caudal* RNA binding within the cytoplasm. To test whether these processes alter Bcd dynamics, we generated eGFP::Bcd^{N51A} (Figure 2A). These embryos show a clear anterior-to-posterior gradient of Bcd (Figure 2B).

We performed FCS on eGFP::Bcd^{N51A} embryos at different locations within n.c. 12-14 embryos. In the nucleus, the normalised autocorrelation curves for eGFP::Bcd^{N51A} embryos are clearly different from eGFP::Bcd embryos, with faster dynamics (Figure 2C-E). However, the dynamics in the cytoplasm are not significantly altered (Figure 2C'-E'). The effective diffusion coefficients further reveal that the diffusion of eGFP::Bcd^{N51A} in the anterior nuclei is 7-9 $\mu m^2/s$ and in the posterior it is 9-13 $\mu m^2/s$ (Figure 2E, Table S3).

In the nucleus, both the fast and slow modes in eGFP::Bcd^{N51A} embryos show increased diffusivity compared to eGFP::Bcd embryos (Figure 2F-F', compared with Figure 1G-G'). While the increase in the slow mode was expected, the reason for the change in the fast mode is less clear. These effects are apparent in both the anterior and posterior of the embryo (Figure S3). As with eGFP::Bcd, the slow mode diffusivity in eGFP::Bcd^{N51A} embryos is similar across the embryo (Figure 2F'), with the fast component increasing towards the posterior (Figure 2F). The relative fraction of eGFP::Bcd^{N51A} in the slow and fast modes also changes from anterior to posterior (Figure 2G), with a larger fraction of eGFP::Bcd^{N51A} being in the faster diffusive mode within the posterior nuclei. These results suggest that (i) Bcd DNA binding plays an important role in determining Bcd dynamics within the nucleus and (ii) the dynamics of Bcd within the nucleus are more complicated than a simple model of bound versus unbound Bcd.[23] This might point towards anomalous diffusion as the dominant diffusive mode,[40] in which instead of two distinct diffusion components, the diffusion coefficient is scale dependent. In fact, the anomaly parameter can provide a good empirical measure for changes in molecular interactions.[23,41] However, the anomalous and two-component fit cannot be easily differentiated and the two-component model provides a simpler model and clearer interpretation of the changes due to binding.

The Bcd homeodomain regulates protein dynamics in both the nucleus and cytoplasm

Bcd dynamics show distinct modes in both the cytoplasm and the nucleus. Given the presence of DNA binding sites, RNA binding elements and putative cytoplasmic interaction sites[37,38,42-45] we hypothesised that the Bcd homeodomain is critical in determining the Bcd kinetics.

To remove the effects of other Bcd domains, we fused the *bcd* homeodomain to eGFP::NLS, which we refer to as eGFP::NLSbcd^{HD} (Figure 3A). We compared the dynamics of this construct with eGFP::NLS. We predicted that, if the homeodomain is an active factor in regulating Bcd dynamics, then eGFP::NLSbcd^{HD} embryos will show slower dynamic modes compared to eGFP::NLS. We observed a clear reduction in protein dynamic modes in both the cytoplasm and nucleus (Figure 3B-D', Figure S4). Interestingly, there were no anterior-posterior differences in the diffusion coefficients of eGFP::NLSbcd^{HD} embryos (Figure 3E, Figure S4B). This is consistent with NLS only weakly interacting with other components. This supports the conclusion that the anterior-posterior dynamic changes are due to interactions of the Bcd protein (from outside the homeodomain) with itself or other elements, and not, for example, due to differences in the physical environment between the anterior and posterior. For eGFP::NLSbcd^{HD} the slow and fast populations represented roughly 50% each at all positions within the embryos (Figure 3F). There is ~3.5-4.5 fold decrease in the effective diffusion coefficients of eGFP::NLS upon addition of the homeodomain to NLS encompassing ~2.5 fold decrease in both D_{fast} and D_{slow} values (Figure S4C-E). Further, the fraction of eGFP::NLSbcd^{HD} in the slower form (F_{slow}) significantly increased compared to eGFP::NLS (compare Figure S2I and Figure 3F).

Bcd binds to *caudal* mRNA to suppress production of Caudal in the embryo, thereby generating a posterior-to-anterior gradient of Caudal.[44] The *caudal* mRNA binding domain on Bcd is within the Bcd homeodomain.[46] To test the role of interactions between Bcd and *caudal* mRNA we generated eGFP::Bcd^{R54A} lines (Figure S5). This mutation in Bcd inhibits the repressive effects of Bcd on *caudal*. This is a weaker Bcd allele than N51A, as *hunchback* transcription is unaffected.[39] We used FCS to probe the Bcd dynamics in eGFP::Bcd^{R54A} embryos and compared with eGFP::Bcd embryos (Figure S5). We observed no significant changes in the Bcd dynamics in eGFP::Bcd^{R54A} embryos (Figure S5D-D'). There still existed an increase in the fast component of the Bcd diffusivity towards the embryo posterior (Figure S5F). In the nucleus, there was a small increase in the slow diffusive components towards the posterior (Figure S5F'). Overall, combined with our results for the N51A allele, this suggests that: (1) the Bcd homeodomain plays an important role in determining Bcd dynamics; (2) Bcd binding to *caudal* mRNA alone is insufficient to explain the Bcd cytoplasmic dynamics; and (3) there are likely other components (either within Bcd itself or other proteins) that affect Bcd dynamics at different Bcd concentrations.

Formation of the Bcd gradient with multiple dynamic modes

Given that there exist distinct dynamic modes for Bcd transport across the embryo, we considered the effects of these on long-range gradient formation for our different constructs (Figure 4A). Before focusing on Bcd, we first analysed the gradient of nuclear eGFP::NLS with and without the *bcd* homeodomain. We see that addition of the homeodomain leads to a substantially shorter intensity profile (Figure 4B). Remarkably, adding the Bcd homeodomain to generate eGFP::NLSbcd^{HD} results in a gradient similar to the eGFP::Bcd gradient (Figure 4B).

With such quantitative data, we developed a diffusive model for the formation of the eGFP::NLS and eGFP::NLSbcd^{HD} gradients. As our focus is on the formation of the long-range gradient, we do not consider differences between nuclei and cytoplasmic transport. We started with the eGFP::NLS; this can be approximately described by a one-component reaction-diffusion model, whereby the protein is produced at a localised source region before diffusing and eventually decaying (Methods). With this, we can replicate the observed gradient, with the inclusion of a degradation term (Figure 4B). To describe the eGFP::NLSbcd^{HD} profile, we considered an effective diffusion, representing the combined fast and slow forms (Methods). By simply altering the effective diffusion, we see that the change in gradient of eGFP::NLSbcd^{HD} embryos is consistent with a reaction-diffusion model of gradient formation, without changing the degradation rate of eGFP::NLS (Figure 4B).

Given the above observations, we next asked how the Bcd gradient itself forms given: (1) it has multiple dynamic modes that vary across the embryos; and (2) within the first 300 μm of the gradient its profile is similar to eGFP::NLSbcd^{HD}. There are (at least) four effective modes of Bcd transport: (1) fast cytoplasmic fraction; (2) slow cytoplasmic fraction; (3) fast nuclear localised fraction; and (4) slow nuclear localised fraction (which is largely due to Bcd DNA binding) (Figure 4C). We know the fractions in each population in the anterior and posterior of the embryo (Figure 1H). As our focus here is on the long-range establishment of the Bcd morphogen gradient, we considered the nuclear bound fraction to be stationary, and considered the cytoplasmic component. This assumption is supported by work showing that the Bcd gradient can form with substantially reduced Bcd nuclear import.[47] To implement the spatially varying diffusion coefficient, we consider $D_{s,f}(x) = D^0_{s,f}\left(1+\frac{x}{x_0}\right)$ for both slow and fast cytoplasmic components. It is likely this is really a function of concentration (discussed below), but we use this linear form for simplicity. To account for the changes in the fraction in the slow and fast forms across the embryo, we consider the rate, β of transition from fast to slow forms to behave as $\beta(\rho_T) = \beta_0 \frac{\rho_T}{\rho_T+\rho_0}$ where $\rho_T = \rho_s + \rho_f$ is the total amount of Bcd at each position, ρ_s and ρ_f are the slow and fast forms of Bcd concentration respectively, and β_0 , ρ_0 are constants.

Applying these assumptions, leads to the coupled differential equations

$$\frac{\partial \rho_s(x,t)}{\partial t} = \frac{\partial}{\partial x}\left(D_s(x)\frac{\partial}{\partial x}\rho_s(x,t)\right) - \mu_s\rho_s(x,t) - \alpha\rho_s(x,t) + \beta(\rho_T)\rho_f(x,t)$$

$$\frac{\partial \rho_f(x,t)}{\partial t} = \frac{\partial}{\partial x}\left(D_f(x)\frac{\partial}{\partial x}\rho_f(x,t)\right) - \mu_f\rho_f(x,t) + \alpha\rho_s(x,t) - \beta(\rho_T)\rho_f(x,t)$$

where $\mu_{s,f}$ denotes the degradation rate for the slow and fast forms and α is the rate of slow-to-fast transition. For simplicity we keep all parameters constant that are not explicitly highlighted as having a functional dependence. Implementing parameters based on our above and other *in vivo* measurements[28,29,48] we can plot the Bcd gradient as a function of time and position (Figure 4D). From this, we see three important points: (1) having the two forms leads to more rapid gradient formation at larger distances; (2) the increased fraction in the fast form results in increased concentration in the posterior; and (3) the steady-state gradient in the

domain [0 μm, 300 μm] is similar across different conditions, consistent with the observations on eGFP:: bcd^{HD}NLS. Even with the multiple species and varying diffusion, the gradient is still exponential across a large extent (black dashed line, Figure 4D), consistent with experimental observations.[4] Yet, importantly, we see increased concentration in the posterior for our concentration-dependent model compared with the SDD model, consistent with experimental observation of Bcd in the most posterior.[49]

Discussion

We have provided a detailed analysis of morphogen dynamics in both space and time. The FCS measurements are consistent with eGFP::Bcd having highly motile and slower fractions, in both the nucleus and the cytoplasm. In the nucleus, the two populations can be largely (though not completely) explained by Bcd binding to DNA. In the cytoplasm, interactions with *caudal* mRNA do not seem to play a major role in determining Bcd dynamics. It is possible that Bcd interacts with cytoplasmic elements, including actin and microtubule structures,[50] which alter its diffusivity. The ability to transform the eGFP::NLS gradient into one that qualitatively matches the eGFP::Bcd gradient through the addition of the Bcd homeodomain suggests that this region of Bcd is critical in determining Bcd dynamics. Given the changing fractions of the fast and slow populations along the embryo, the interactions between the populations are likely non-linear, and dependent on the local eGFP::Bcd concentration.

Our results help to resolve several observations regarding eGFP::Bcd dynamics. First, FRAP measurements of eGFP::Bcd in the cytoplasm have reported an effective diffusion coefficient in the range $0.3 - 1\ \mu m^2/s$.[4,29] Our measurements of the cytoplasmic slow fraction (D_{slow}~$1 \mu m^2/s$) are consistent with this. This suggests that the dynamics of the fast fraction were not captured by previous FRAP measurements. Second, single molecules of eGFP::Bcd have been observed in the embryo posterior.[24] Even with an effective diffusion coefficient of $7\ \mu m^2/s$, few molecules would be expected at the posterior given the estimated Bcd lifetime (30-50 minutes). However, we show that eGFP::Bcd in its fastest form can move quickly ($\sim 18\ \mu m^2/s$), and the fraction of eGFP::Bcd in this form increases at lower concentrations. Therefore, it is possible for a subpopulation of eGFP::Bcd to reach the posterior, while the majority of eGFP::Bcd forms a steep concentration profile (Figure 4D). This is consistent with theoretical predictions, that also postulated that Bcd may have spatially varying dynamics.[30] Bcd maintains a similar profile across multiple nuclear cycles.[4] The presence of a rapidly diffusing pool can (at least partially) help to re-establish the gradient quickly after each division. Finally, it has been proposed that Bcd can be produced throughout the embryo, without need for long-ranged diffusive transport.[12] Yet, our results suggest that >50% of eGFP::Bcd exists in a rapidly diffusing form ($D > 5\ \mu m^2/s$), which will "wash out" a locally produced gradient.

Such spatially varying dynamics have been hypothesised previously.[51] The subcellular gradient of Mex-5 within the *C. elegans* embryo has spatially varying dynamics, due to interactions mediated by polarised distribution of PAR proteins[52] and a recent study in *Xenopus* extracts has shown that cytoplasmic organisation can alter protein diffusivity.[53] In our case, the specific

mechanism of dynamic change is not clear. There are not known significant structural differences in the anterior and posterior ends of the embryo at this stage nor are there gradients of polarity. Our results suggest that the Bcd homeodomain has a role in regulating the protein dynamics in the cytoplasm. Bcd binds to the BRE (Bicoid response element) in the caudal 3'UTR and it also binds to the 5'CAP of the caudal mRNA through its PEST domain via adaptor proteins.[39,44,54,55] Therefore, our mutants may only have partial loss of Bcd binding to the *caudal* RNA in the cytoplasm. Future work could explore mutations in both the homeodomain (N51A) and the PEST domain. Bcd may also bind to cytoskeletal elements that alter the dynamics. Alternatively, if *caudal* binding is the dominant factor slowing Bcd in the posterior, we predict that there should be a larger fraction of Bcd in the slow population in *caudal* over-expressing embryos. There are additional factors, such as Zelda, that may also play a role in spatially varying the effective Bcd dynamics.[47] Finally, our above results suggest that the transition between the slow and fast cytoplasmic forms may depend non-linearly on the local Bcd concentration. More refined spatial dissection of the dynamics may help illuminate this behaviour more clearly.

We have used dual colour imaging to ensure that we are recording accurately either nucleus or cytoplasmic pools. An alternative strategy is to use imaging-FCS.[21] With this approach, the available timescales are reduced (lowest time resolution about 0.1 ms) but spatial cross-correlation can be explored.[21] This approach also has the advantage of being able to image throughout mitosis, as spatial movements of the nuclei can be accounted for. It will be interesting to explore how Bcd dynamics change during nuclear division in the blastocyst.

Overall, the combination of new reagents with careful FCS measurements has revealed insights into how a morphogen gradient can form across the required spatial and temporal scales. Outstanding questions include: (1) what interactions are determining Bcd dynamics in the cytoplasm; (2) is Bcd diffusivity concentration-dependent, and if so how; and (3) whether other morphogens display position/concentration dependent dynamics?

Acknowledgements

This work was funded by a Singapore MOE Tier 3 grant (MOE2016-T3-1-005) to TW and TES and a Singapore MOE Tier 2 grant (MOE2018-T2-2-138) to TES. TES was also supported by an EMBO Global Investigator award and start-up support from University of Warwick, UK. CB was funded by the Global Fellows Program of the College of Agriculture and Life Sciences, Cornell University, USA.

Author Contributions

TES initiated the project with proof-of-principle data collected by CB. TA performed all the experiments shown here with assistance from AVSN, under the supervision of TW and TES. TA performed the data analysis with support from TW and TES. TA, TW and TES wrote the first draft of the manuscript, with all authors contributing to the final submitted version.

Methods

Generation of fly lines

eGFP::Bcd fly line was a gift from Thomas Gregor.[4] The eGFP::Bcd line was generated by introducing eGFP coding region into the N-terminus of the *bcd* coding region after the start codon in the pCaSpeR7 Bcd plasmid.[56-58] eGFP tagged Bcd was brought in the background of bcd^{1} null allele to ensure that it is the only source of Bcd in these embryos. eGFP::Bcd was crossed with His2A::mCherry[59] to mark the nuclei of early blastoderm embryos, such that the 560-laser line could act as a reference to mark the nucleus and to differentiate the cytoplasmic region in the syncytium. eGFP::Bcd^{N51A} and eGFP::Bcd^{R54A} mutant lines were generated by introducing point mutations at specific locations in the homeodomain of the eGFP::Bcd pCaSpeR7 construct using primers bearing appropriate base pair changes.

For control, we generated an eGFP::NLS line expressed using the Bcd regulatory sequences.[60] We introduced a nuclear localisation sequence and a stop codon at the end of the eGFP sequence in the eGFP::Bcd pCasper7 plasmid as described in Ref. 60. Upon translation, the eGFP::NLS generated a gradient expression across the A-P axis of the embryo (Figure S2A; Figure 4A). For generating eGFP::NLSbcd^{HD} line, we introduced the homeodomain sequence of Bcd that codes for 60 aminoacids. We PCR amplified the 180 bp homeodomain sequence from exon 3 of the Bcd genomic region using primers that had a GS_6 linker and Kpn1 restriction site at their extreme ends. The Kpn1-GS_6-bcd^{HD}-GS_6 –Kpn1 fragment was digested and inserted into the newly introduced Kpn1 site of the acceptor eGFP::NLS plasmid.

Preparation of embryos for FCS measurements

eGFP::Bcd; His2A::mCherry embryos at n.c. 9 were dechorionated and mounted in PBS on a coverslip in such a way that the dorsal surface of the embryo struck to the surface of the coverslip and faced the objective. The cortical planar surface of the embryo, which contained the maximum number of in-focus nuclei, was selected for FCS measurements (Figure 1A). His2A::mCherry marked nuclei was used as a reference for the nuclear Bcd FCS measurements, and the area devoid of His2A::mCherry was used for the cytoplasmic Bcd measurements.

FCS conditions:

Fluorescence Correlation Spectroscopy (FCS) was carried out using a FV1200 confocal microscope (Olympus) equipped with a time-resolved FCS upgrade kit (PicoQuant) at 25^{0}C. The 488 nm pulse wave laser line was used to excite eGFP::Bcd through an UplanSApo 60 X NA 1.2 water immersion objective (Olympus). The laser power was optimised using nuclear eGFP::Bcd at n.c. 14. Laser powers of 2-3µW, which had better signal to noise ratio and minimal photobleaching, were used for FCS measurements both in the nucleus and cytoplasm regions of the anterior and posterior domains of the embryo (Methods Figure 1). The fluorescence emission was passed through a 405/488/543/635 dichroic mirror (Chroma Technology), confocal pinhole of one airy unit (120 µm), and then split using a 50/50 mirror plate. The split emission was detected simultaneously by an avalanche photodiode (SPCM-AQR14; PerkinElmer). Dual detector measurements effectively remove after-pulsing information in the FCS curves. The photon counts from the detector were registered by a TimeHarp 260 time-correlated single photon counting board (PicoQuant) and processed by the

SymPhoTime [64] software (PicoQuant). The same software was also used to calculate the cross-correlation function.

Calibration of FCS measurements:

We calibrated eccentricity of the confocal volume, κ before each round of measurements using the reference dye Atto-488 (Atto-Tec) that has a diffusion coefficient 400 $\mu m^2/s$ at room temperature.[61] The effective volume of calibration (V_{eff}, from picoquant) was found to be 0.25±0.04fl and the value of κ was found to be 5.6±0.9. The value for κ was fixed at 5.6.

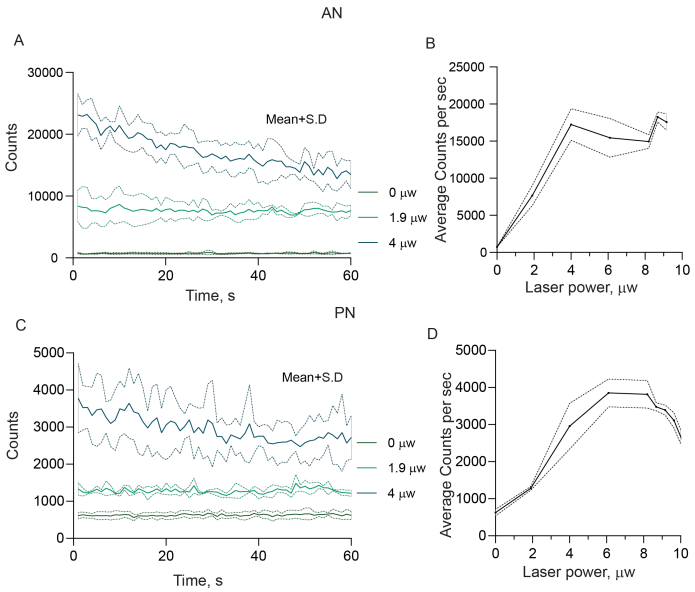

Methods Figure 1: Laser power optimisation *(A, C) line plot showing the time trace of the eGFP:Bcd in the anterior (A) and posterior nuclei (C). Mean (solid line) and SD (dotted line) of the time trace are shown for laser powers 0, 1.9 and 4µw. (B, D) Mean counts per sec increases with laser power and gets saturated above laser power of 4µw due to photobleaching.*

Estimation of eGFP::Bcd concentration in the measurement volume:

We estimated the concentration of eGFP::Bcd and eGFP::NLS through generating a standard curve (Method Figure 2). A high known concentration of Atto-488 dye was serially diluted to lower concentrations (10, 7, 5, and 2 nM) and the correlation amplitudes determined. A plot of the inverse of correlation amplitude *i.e.,* the number of molecules vs concentration in nM fit a linear line (Methods Figure 2B). The unknown concentrations of eGFP::Bcd and eGFP::NLS in the embryos were found from the line equation shown in Methods Figure 2B.

Qualitative comparison of ACF curves:

ACF curves of individual measurements were normalised and compared to show their qualitative differences. The ACF curves were normalised using the formula $G(\tau) - G(\infty)/G(0) - G(\infty)$. G (0) is the amplitude of the ACF curves (typically at lag time 0.0001s), G (∞) is the convergence value at the longer lag times (typically 1s).

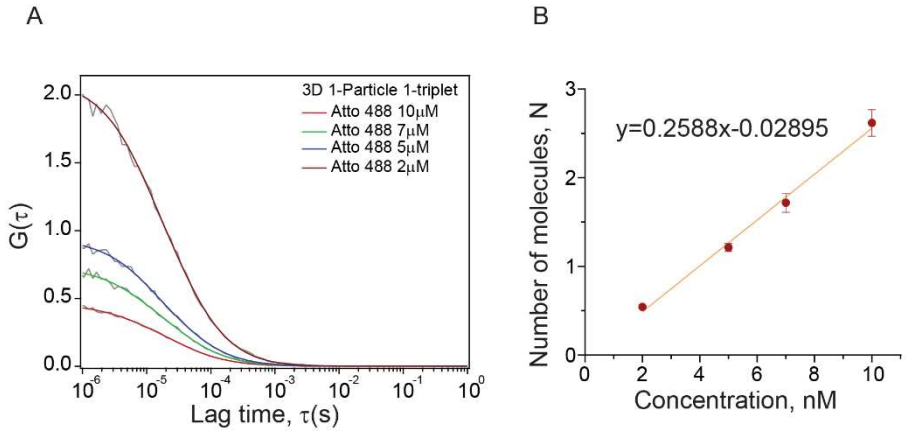

Method Figure 2: calibration of effective volume to estimate the concentration *(A) Normalised ACF curves (grey) of Atto-488 of different concentration and the 1-particle 1-triplet fits. (B) linear increase in number of molecules in the confocal volume upon increasing the concentration of Atto-488 (2,5,7, and 10nM).*

FCS curve Fitting:

The FCS curves of each measurement were fitted by 3-dimensional diffusion models involving diffusion of 1 and 2 species with and without reversible switching of the fluorophores to dark states, using Igor-Pro (8.03), FCS data processing plugin, Version 2.1, based on Refs 58, 60 and 61. The 3D model involving diffusion of 2 species was selected as it provided a good fit determined through quality of the residuals of each plot.[29] Photophysical processes, *e.g.*, triplet transitions (Atto488) or photoisomerisation and protonation kinetics (eGFP) at short times[62] are a concern when estimating accurate diffusion times. The error rate in the measurement of the diffusion time becomes worse if the characteristic times of photophysical processes are large enough to overlap with the diffusion time. Further, since the brightness eGFP:Bcd in the anterior and posterior cytoplasm is lower compared to the nuclei, the noise in these curves further limits the distinction between photophysics and diffusion, reducing the accuracy of the determined τ_D values.

Therefore, we fitted our FCS curves with different time ranges to include or exclude the photophysical processes at short times. A lag time range of 0.001ms to 1s was considered for fits including photophysics and 0.1 ms to 1 s for fits excluding photophysics. The photophysical parameters, denoted for simplicity as τ_{trip} for the characteristic time and F_{trip} for the fraction, were allowed to vary. Comparable τ_{D1} and τ_{D2} values of fits in- or excluding photophysics of each curve were selected. Our estimation reveals comparable photophysics parameters values across the A-P axis (Method Figure 3). The majority of the $\boldsymbol{\tau_{triplet}}$ values range from 0.03 to 0.08ms (30 to 80μs) is comparable to the characteristic times of eGFP measured previously.[63,64] The fraction ranges from 0.15 to 0.22 (Method Figure 3). The data with anomalies due to photobleaching or sudden jumps in the intensities due to movement of the nucleus during measurements, were excluded from evaluation.

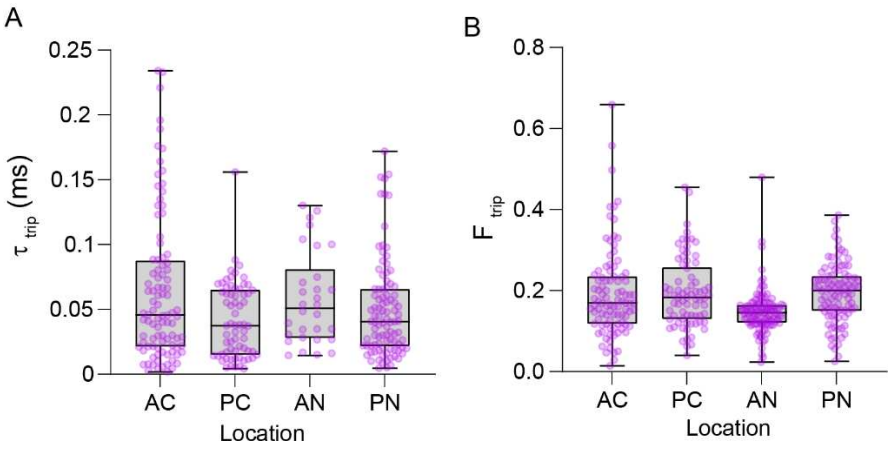

Method Figure 3: Estimation of triplet lifetime, $\tau_{triplet}$ and its fraction ($F_{triplet}$): *(A) Box-whisker plot showing the values of the characteristic times of photophysical processes, $\tau_{triplet}$, from multiple ACF curves measured from 4 embryos, across all compartments. The fraction (F_{trip})is given in B. AC- anterior cytoplasm, PC-posterior cytoplasm, AN-anterior nuclei, and PN-posterior nuclei.*

Quantification of eGFP::Bcd* and *eGFP::NLS gradients:

Time lapse videos of embryos at n.c. 14 were acquired along the longitudinal plane passing through midline of the embryo. For each embryo, two separate images of size 512x512 pixels along the mid sagittal plane covering anterior and posterior domains of the embryo were stitched together. The images were captured at 8bits/pixel, pixel dwell time of 3 µs, line averaging 4, 5 Z-sections of thickness 1 µm each. The conditions captured maximum in-focus peripheral nuclei along the mid-sagittal plane in the Zeiss LSM 710 confocal scanning microscope. The nuclear eGFP intensities along the embryo circumference at n.c. 14 were measured using plot profile plugin of image J. A line mask along the circumference of the embryo was drawn covering the nuclei. The measured raw intensity profile along the circumference of the embryo was background corrected and plotted against the actual length of the embryo.

Modelling of gradient formation:

For the eGFP::NLS model (Figure 4B), we consider the concentration (ϕ) as,

$$\partial_t \phi(x,t) = D\partial_x^2 \phi(x,t) - \mu\phi(x,t) + Jf(x,x_s)$$

where D is the diffusion coefficient, μ the degradation rate and $Jf(x,x_s)$ defines the production region, and $f(x,x_s) = 1\ if\ x < x_s$ and 0 otherwise. Boundary conditions $\partial_x\phi(x=0,t) = 0$ and $\partial_x\phi(x=L,t) = 0$ were used, where $L = 500\mu m$ represents the embryo length.

For eGFP::Bcd, the equations are given in the main text. All equations solved in 1D using MATLAB pdepe solver with zero flux boundary conditions at x=L.

Figures and legends

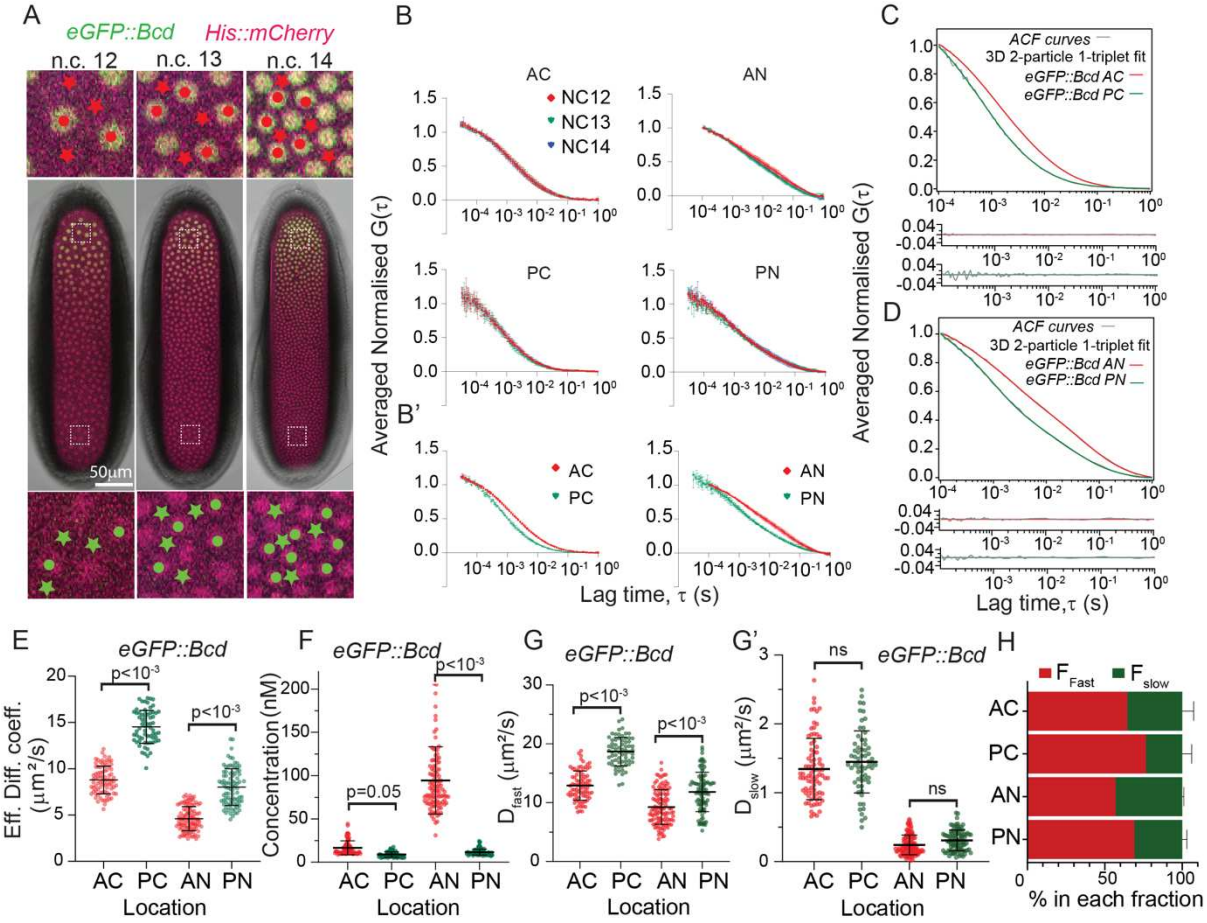

Figure 1: Spatio-temporal dynamics of eGFP::Bcd in the early *Drosophila* embryo

(A) *Drosophila* blastoderm showing the interphase periods of nuclear cycles (n.c.) 12, 13 and 14. Nuclei (mCherry::His2Av, magenta) and eGFP::Bcd (green). Dots and stars indicate cytoplasmic and nuclear regions, respectively, where FCS measurements are carried out in the anterior (red) and posterior (green). (B) Qualitative comparison of normalised and averaged autocorrelation (ACF) curves with mean and S.D. of eGFP::Bcd in the cytoplasmic and nuclear compartments of the n.c. 12,13, and 14 interphases. The anterior and posterior domains are shown in the upper and lower panels respectively. Lag times from 0.0001secs to 1sec are shown. (B') Superimposed cytoplasmic (left) and nuclear ACF (right) curves from the anterior (red) and posterior (green). (C, D) Comparison of ACF curves (grey) with residues fitted with 3D 2-particle 1-triplet diffusion model. The comparisons are shown from 0.0001 sec to 1 sec lag times for visual clarity. Red and green fits correspond to anterior and posterior, respectively. (E-G') Scatter plots comparing: effective diffusion coefficients (E); concentration (F); D_{fast} (G); and D_{slow} (G') of eGFP::Bcd in the anterior cytoplasm (AC), posterior cytoplasm (PC), anterior nuclei (AN), and posterior nuclei (PN). For each condition, multiple measurements are taken from between 3-5 embryos in n.c. 12 to n.c. 14. (H). Bar plots indicating fractions (%) of fast and slow diffusing Bcd molecules in the corresponding embryo compartments. Error bars ±1 s.d. P values calculated using a two-sided permutation test.[65]

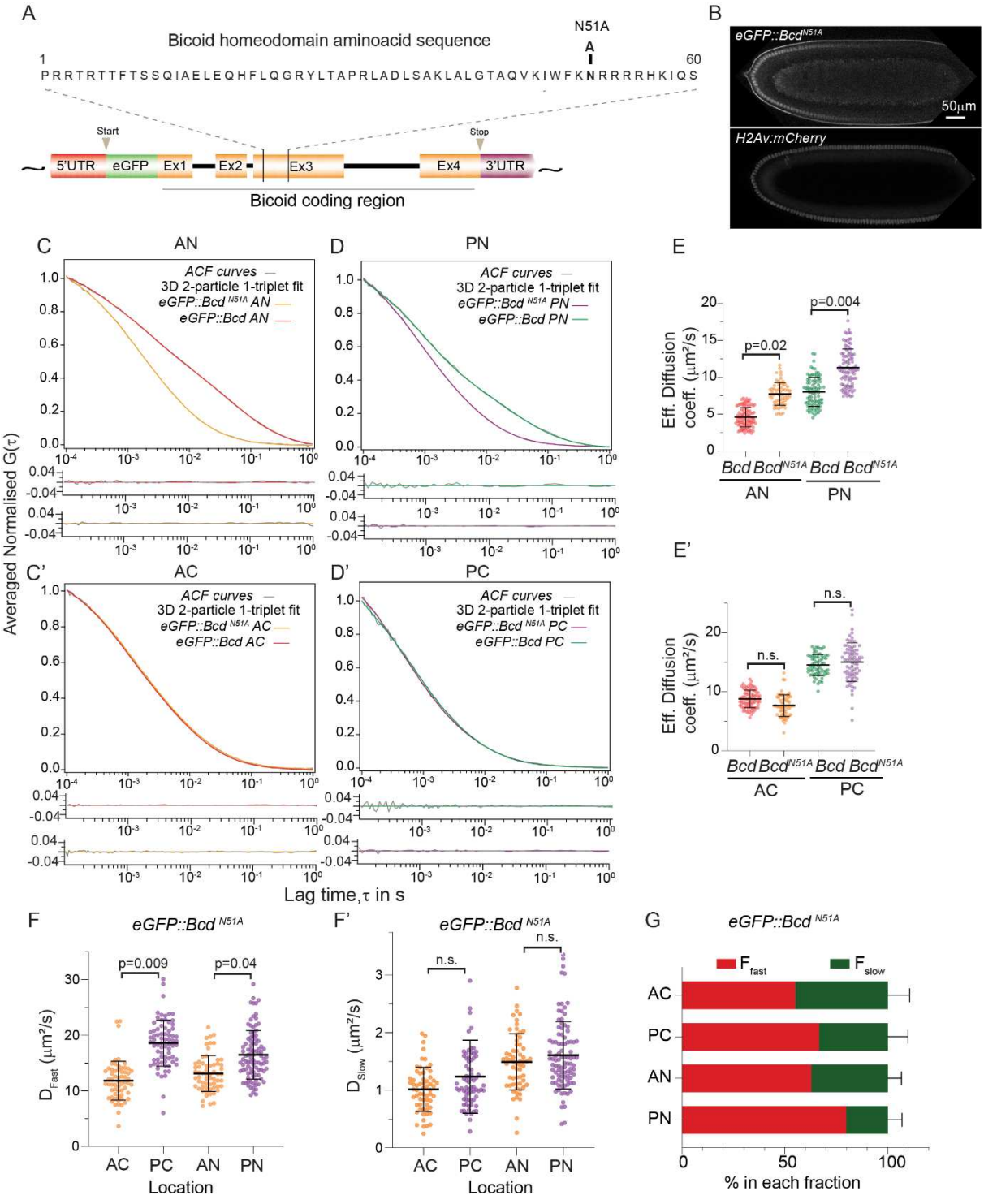

Figure 2: Bcd homeodomain alters nuclear Bcd dynamics

(A) Schematic of *Drosophila bcd* genomic region. 60 amino acids constituting *bcd* homeodomain is expanded. Amino acid conversion at position 51 from asparagine to alanine (N51A) is displayed. (B) Midsagittal section of n.c. 14 *Drosophila* embryo expressing eGFP::Bcd^{N51A} (top) and mCherry tagged histone (bottom). (C-D') Qualitative comparison of averaged normalised ACF curves (grey) of eGFP::Bcd and eGFP::Bcd^{N51A} with residues fitted with 3D 2-particle 1-triplet diffusion model. Red and green fits correspond to nuclear and cytoplasmic regions of anterior and posterior regions of Bcd, respectively. Yellow and purple fits correspond to eGFP::Bcd^{N51A} . (E-E') Comparison of the effective diffusion coefficients of

549 eGFP::Bcd and eGFP::Bcd^{N51A} in the nucleus (E) and cytoplasm (E'). (F-F') Scatter plots
550 comparing D_{fast} (F) and D_{slow} (F') of eGFP::Bcd^{N51A} at different locations within the embryo
551 (labelling as Figure 1E-G'). (G) Bar plots indicating fractions (%) of fast and slow diffusing
552 eGFP::Bcd^{N51A} molecules in the corresponding embryo compartments. P values calculated
553 using a two-sided permutation test.[65] All error bars denote ±1 s.d.
554

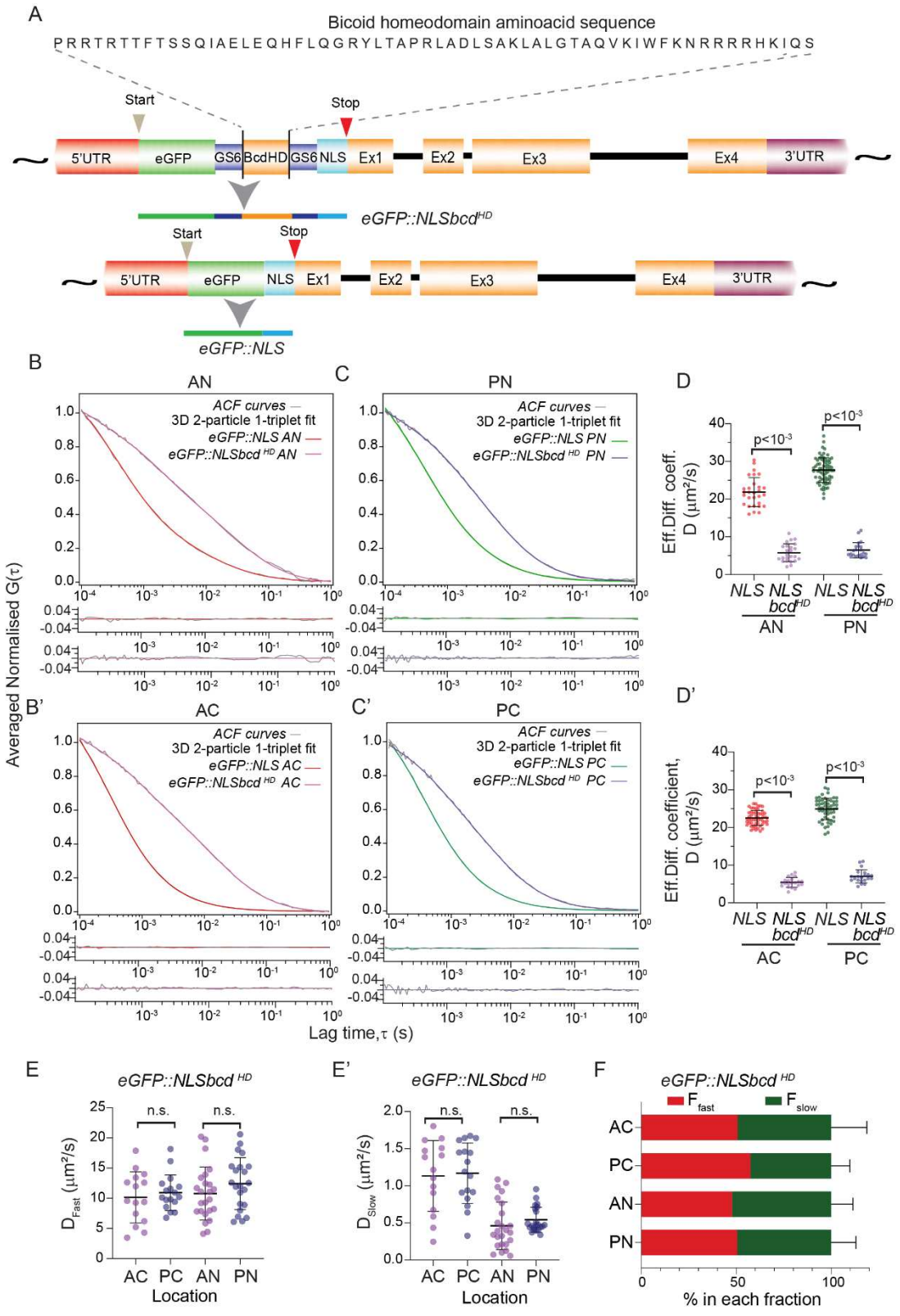

555

Figure 3: Effects on dynamics of adding the *Bcd* homeodomain to NLS

(A) Schematic of the construction of the eGFP::NLS and eGFP::NLSbcd^{HD} lines. The *bcd* homeodomain is inserted between eGFP and NLS flanked by GS6 linker to generate eGFP::NLSbcd^{HD}. (B-C') Comparison of averaged normalised ACF curves (grey) of eGFP::NLS and eGFP::NLSbcd^{HD} with residues fitted with 3D 2-particle 1-triplet diffusion model. Red and green fits correspond to nuclear and cytoplasmic regions of anterior and posterior, respectively. Purple and violet fits correspond to eGFP::NLSbcd^{HD}. (D-D') Comparison of the effective diffusion coefficients of eGFP::NLS and eGFP::NLSbcd^{HD} for nuclei (D) and cytoplasm (D'). (E-E') Scatter plots comparing D_{fast} (E), and D_{slow} (E) for eGFP::NLSbcd^{HD}. (F) Bar plots indicating fractions (%) of fast and slow diffusing eGFP::NLSbcd^{HD} molecules in the corresponding embryo compartments. P values calculated using a two-sided permutation test.[65] All error bars denote ±1 s.d.

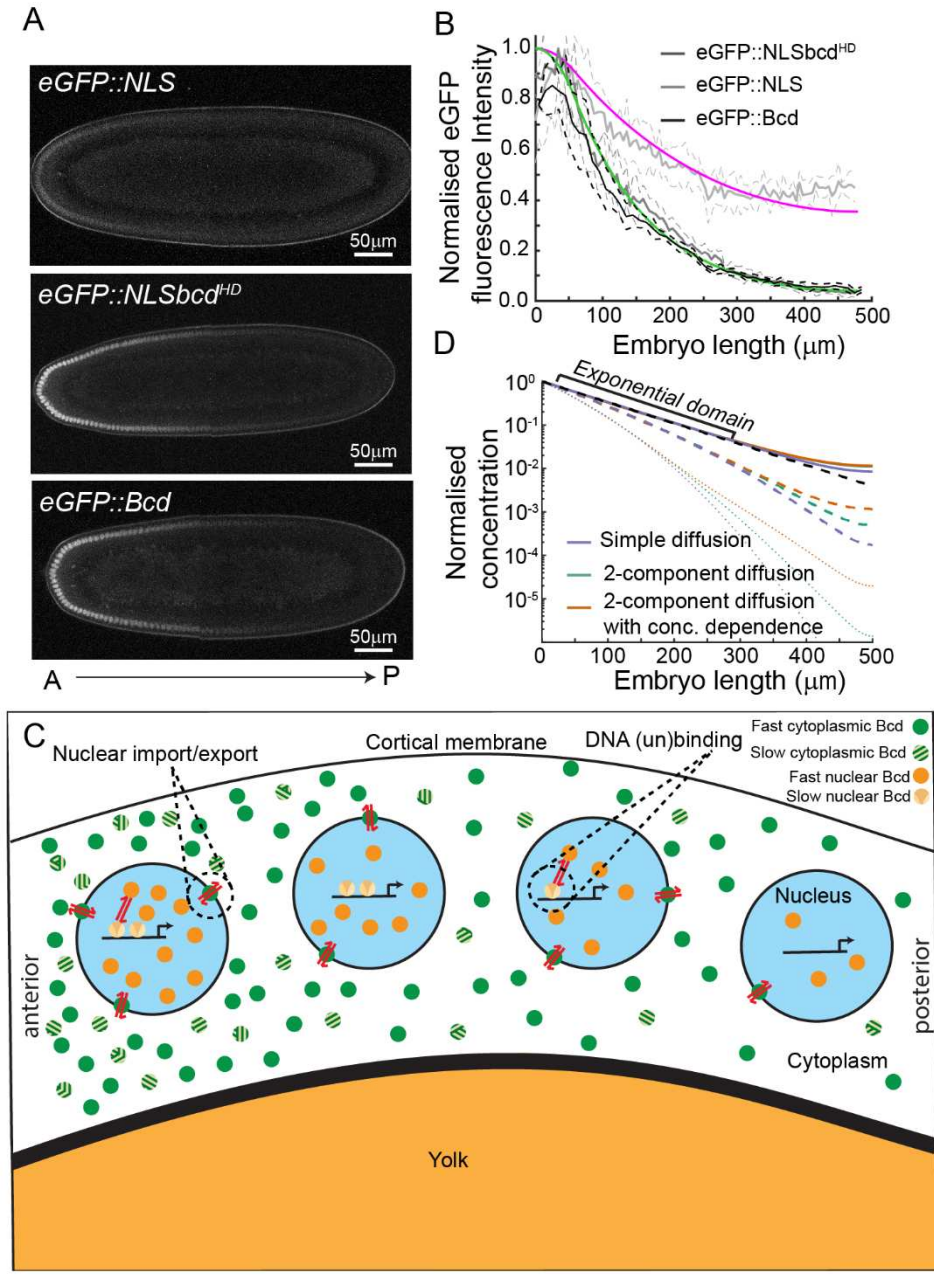

Figure 4: Concentration-dependent parameters within the SDD model can replicate the observed Bcd dynamics and gradient

(A) Midsagittal section of *Drosophila* embryos at n.c.14 expressing eGFP::NLS (top), eGFP::NLSbcd^{HD} (middle), and eGFP::Bcd (bottom). (B) Comparison of normalised gradient profiles between eGFP::NLS (light grey), eGFP::NLSbcd^{HD} (grey) and eGFP::Bcd (black). Model fits (Methods) for eGFP::NLS (magenta), eGFP::NLSbcd^{HD} (green). (C) Schematic of predicted Bcd dynamic modes based on results presented here and existing literature. (D) Model prediction for formation of the Bcd gradient, where we consider a classic SDD model (blue), 2-component diffusion without parameter sensitivity on concentration (green) and 2-component diffusion with concentration dependence in the switching between fast and slow states (orange). Dotted, dashed and solid lines correspond to 10 min, 25 min and 120 min respectively after initiating the simulation (which starts at zero).

Data Availability

Raw data of the ACF curves will be provided on request.

References

1. Wartlick, O., Kicheva, A. & Gonzalez-Gaitan, M. Morphogen Gradient Formation. *CSH Persp. Biol.* **1,** a001255 (2009).
2. Briscoe, J. & Small, S. Morphogen rules: design principles of gradient-mediated embryo patterning. *Development* **142,** 3996 (2015).
3. Kicheva, A. *et al.* Kinetics of Morphogen Gradient Formation. *Science* **315,** 521 (2007).
4. Gregor, T., Wieschaus, E. F., McGregor, A. P., Bialek, W. & Tank, D. W. Stability and Nuclear Dynamics of the Bicoid Morphogen Gradient. *Cell* **130,** 141 (2007).
5. Yu, S. R. *et al.* Fgf8 morphogen gradient forms by a source-sink mechanism with freely diffusing molecules. *Nature* **461,** 533 (2009).
6. Kerszberg, M. & Wolpert, L. Mechanisms for positional signalling by morphogen transport: a theoretical study. *J. Theor. Biol.* **191,** 103 (1998).
7. Kornberg, T. B. Cytonemes and the dispersion of morphogens. *WIREs Dev Biol* **3,** 445 (2014).
8. Stapornwongkul, K. S. & Vincent, J.-P. Generation of extracellular morphogen gradients: the case for diffusion. *Nature Reviews Genetics* **22**, 393 (2021).
9. Huang, A. & Saunders, T. E. A matter of time: Formation and interpretation of the Bicoid morphogen gradient. *Curr. Top. Dev. Biol.* **137,** 79 (2020).
10. Driever, W. & Nüsslein-Volhard, C. A gradient of bicoid protein in Drosophila embryos. *Cell* **54,** 83 (1988).
11. Grimm, O., Coppey, M. & Wieschaus, E. Modelling the Bicoid gradient. *Development* **137,** 2253 (2010).
12. Spirov, A. *et al.* Formation of the *bicoid* morphogen gradient: an mRNA gradient dictates the protein gradient. *Development* **136,** 605 (2009).
13. Ali-Murthy, Z. & Kornberg, T. B. Bicoid gradient formation and function in the Drosophila pre-syncytial blastoderm. *eLife* **5,** e13222 (2016).
14. Roy, S., Huang, H., Liu, S. & Kornberg, T. B. Cytoneme-Mediated Contact-Dependent Transport of the Drosophila Decapentaplegic Signaling Protein. *Science* **343,** 1244624 (2014).

15. Stanganello, E. *et al.* Filopodia-based Wnt transport during vertebrate tissue patterning. *Nat. Comm.* **6,** 5846 (2015).
16. Eldar, A., Rosin, D., Shilo, B. Z. & Barkai, N. Self-enhanced ligand degradation underlies robustness of morphogen gradients. *Dev. Cell* **5,** 635 (2003).
17. Muller, P., Rogers, K. W., Yu, S. R., Brand, M. & Schier, A. F. Morphogen transport. *Development* **140,** 1621 (2013).
18. Saunders, T. & Howard, M. Morphogen profiles can be optimized to buffer against noise. *Phys. Rev. E* **80,** 041902 (2009).
19. He, F. *et al.* Shaping a morphogen gradient for positional precision. *Biophys. J.* **99,** 697–707 (2010).
20. Veerapathiran, S. *et al.* Wnt3 distribution in the zebrafish brain is determined by expression, diffusion and multiple molecular interactions. *eLife* **9,** e59489 (2020).
21. Krieger, J. W. *et al.* Imaging fluorescence (cross-) correlation spectroscopy in live cells and organisms. *Nature Protocols* **10,** 1948 (2015).
22. Wang, Y., Wang, X., Wohland, T. & Sampath, K. Extracellular interactions and ligand degradation shape the nodal morphogen gradient. *eLife* **5,** 91 (2016).
23. Fradin, C. On the importance of protein diffusion in biological systems: The example of the Bicoid morphogen gradient. *BBA - Proteins and Proteomics* **1865,** 1676 (2017).
24. Mir, M. *et al.* Dynamic multifactor hubs interact transiently with sites of active transcription in Drosophila embryos. *eLife* **7,** e40497 (2018).
25. Kuhn, T. *et al.* Single-molecule tracking of Nodal and Lefty in live zebrafish embryos supports hindered diffusion model. *bioRxiv* 2022.04.05.487143 (2022).
26. Khmelinskii, A. *et al.* Tandem fluorescent protein timers for in vivo analysis of protein dynamics. *Nat Biotechnol* **30,** 708 (2012).
27. Donà, E. *et al.* Directional tissue migration through a self-generated chemokine gradient. *Nature* **503,** 285 (2014).
28. Durrieu, L. *et al.* Bicoid gradient formation mechanism and dynamics revealed by protein lifetime analysis. *Mol Sys Biol* **14,** e8355–15 (2018).
29. Abu-Arish, A., Porcher, A., Czerwonka, A., Dostatni, N. & Fradin, C. High mobility of bicoid captured by fluorescence correlation spectroscopy: implication for the rapid establishment of its gradient. *Biophys. J.* **99,** L33 (2010).
30. Sigaut, L., Pearson, J. E., Colman-Lerner, A. & Ponce Dawson, S. Messages Do Diffuse Faster than Messengers: Reconciling Disparate Estimates of the Morphogen Bicoid Diffusion Coefficient. *PLoS Comput Biol* **10,** e1003629 (2014).
31. Muller, P. *et al.* Differential Diffusivity of Nodal and Lefty Underlies a Reaction-Diffusion Patterning System. *Science* **336,** 721 (2012).
32. Lord, N. D., Carte, A. N., Abitua, P. B. & Schier, A. F. The pattern of nodal morphogen signaling is shaped by co-receptor expression. *eLife* **10,** 54894 (2021).
33. Stapornwongkul, K. S., de Gennes, M., Cocconi, L., Salbreux, G. & Vincent, J.-P. Patterning and growth control in vivo by an engineered GFP gradient. *Science* **370,** 321 (2020).
34. Little, S. C., Tkačik, G., Kneeland, T. B., Wieschaus, E. F. & Gregor, T. The Formation of the Bicoid Morphogen Gradient Requires Protein Movement from Anteriorly Localized mRNA. *PLoS Biol* **9,** e1000596 (2011).
35. Porcher, A. *et al.* The time to measure positional information: maternal Hunchback is required for the synchrony of the Bicoid transcriptional response at the onset of zygotic transcription. *Development* **137,** 2795 (2010).
36. Driever, W. & Nüsslein-Volhard, C. The bicoid protein determines position in the Drosophila embryo in a concentration-dependent manner. *Cell* **54,** 95 (1988).

37. Burz, D. S., Rivera-Pomar, R., Jäckle, H. & Hanes, S. D. Cooperative DNA-binding by Bicoid provides a mechanism for threshold-dependent gene activation in the Drosophila embryo. *EMBO J* **17,** 5998 (1998).
38. Lebrecht, D. *et al.* Bicoid cooperative DNA binding is critical for embryonic patterning in Drosophila. *Proc. Natl. Acad. Sci. U.S.A.* **102,** 13176 (2005).
39. Niessing, D. *et al.* Homeodomain position 54 specifies transcriptional versus translational control by Bicoid. *Mol Cell* **5,** 395 (2000).
40. Höfling, F. & Franosch, T. Anomalous transport in the crowded world of biological cells. *Rep. Prog. Phys.* **76,** 046602 (2013).
41. Furlan, A. *et al.* HEXIM1 Diffusion in the Nucleus Is Regulated by Its Interactions with Both 7SK and P-TEFb. *Biophys. J.* **117,** 1615 (2019).
42. Ma, X., Yuan, D., Diepold, K., Scarborough, T. & Ma, J. The Drosophila morphogenetic protein Bicoid binds DNA cooperatively. *Development* **122**, 1195 (1996).
43. Yuan, D., Ma, X. & Ma, J. Sequences Outside the Homeodomain of Bicoid Are Required for Protein-Protein Interaction. *Journal of Biological Chemistry* **271,** 21660 (1996).
44. Niessing, D., Dostatni, N., Jäckle, H. & Rivera-Pomar, R. Sequence interval within the PEST motif of Bicoid is important for translational repression of caudal mRNA in the anterior region of the *Drosophila* embryo. *EMBO J* **18,** 1966 (1999).
45. Ling, J., Umezawa, K. Y., Scott, T. & Small, S. Bicoid-Dependent Activation of the Target Gene hunchback Requires a Two-Motif Sequence Code in a Specific Basal Promoter. *Mol Cell* **75,** 1178 (2019).
46. Rivera-Pomar, R., Niessing, D., Schmidt-Ott, U., Gehring, W. J. & Jäckle, H. RNA binding and translational suppression by bicoid. *Nature* **379,** 746 (1996).
47. Grimm, O. & Wieschaus, E. The Bicoid gradient is shaped independently of nuclei. *Development* **137,** 2857 (2010).
48. Drocco, J. A., Grimm, O., Tank, D. W. & Wieschaus, E. Measurement and perturbation of morphogen lifetime: effects on gradient shape. *Biophys. J.* **101,** 1807 (2011).
49. Mir, M. *et al.* Dense Bicoid hubs accentuate binding along the morphogen gradient. *Genes & Development* **31,** 1784 (2017).
50. Cai, X., Akber, M., Spirov, A. & Baumgartner, S. Cortical movement of Bicoid in early Drosophila embryos is actin- and microtubule-dependent and disagrees with the SDD diffusion model. *PLoS ONE* **12,** e0185443 (2017).
51. Lipkow, K. & Odde, D. J. Model for Protein Concentration Gradients in the Cytoplasm. *Cel. Mol. Bioeng.* **1,** 84 (2008).
52. Griffin, E. E., Odde, D. J. & Seydoux, G. Regulation of the MEX-5 gradient by a spatially segregated kinase/phosphatase cycle. *Cell* **146,** 955 (2011).
53. Huang, W. Y. C., Cheng, X. & Ferrell, J. E. Cytoplasmic organization promotes protein diffusion in Xenopus extracts. *Nat. Comm.* **13,** 5599 (2022).
54. Niessing, D., Blanke, S. & Jäckle, H. Bicoid associates with the 5'-cap-bound complex of caudal mRNA and represses translation. *Genes & Development* **16,** 2576 (2002).
55. Macdonald, P. M. Translational repression by Bicoid: competition for the cap. *Cell* **121,** 321 (2005).
56. Thummel, C. S. & Pirrota, V. New pCaSpeR P-element vectors. *Drosophila information service* **71,** 150 (1992).
57. Hazelrigg, T., Liu, N., Hong, Y. & Wang, S. GFP expression in Drosophila tissues: time requirements for formation of a fluorescent product. *Dev. Biol.* **199,** 245 (1998).

58. Barolo, S., Carver, L. A. & Posakony, J. W. GFP and beta-galactosidase transformation vectors for promoter/enhancer analysis in Drosophila. *BioTechniques* **29,** 727 (2000).
59. Krzic, U., Gunther, S., Saunders, T. E., Streichan, S. J. & Hufnagel, L. Multiview light-sheet microscope for rapid in toto imaging. *Nat Meth* **9,** 730 (2012).
60. Gregor, T., McGregor, A. P. & Wieschaus, E. F. Shape and function of the Bicoid morphogen gradient in dipteran species with different sized embryos. *Dev. Biol.* **316,** 350 (2008).
61. Kapusta, P. Absolute Diffusion Coefficients: Compilation of Reference Data for FCS Calibration. *PicoQuant Application Note* (2011).
62. Widengren, J., Mets, Ü. & Rigler, R. Photodynamic properties of green fluorescent proteins investigated by fluorescence correlation spectroscopy. *Chemical Physics* **250,** 171 (1999).
63. Haupts, U., Maiti, S., Schwille, P. & Webb, W. W. Dynamics of fluorescence fluctuations in green fluorescent protein observed by fluorescence correlation spectroscopy. *Proc. Natl. Acad. Sci. U.S.A.* **95,** 13573 (1998).
64. Jiménez-Banzo, A., Nonell, S., Hofkens, J. & Flors, C. Singlet oxygen photosensitization by EGFP and its chromophore HBDI. *Biophys. J.* **94,** 168 (2008).
65. Ho, J., Tumkaya, T., Aryal, S., Choi, H., Claridge-Chang, A. Moving beyond P values: data analysis with estimation graphics. Nature Methods **16**, 565 (2019).